Chemical Science

ROYAL SOCIETY OF CHEMISTRY

EDGE ARTICLE

View Article Online
View Journal | View Issue

Cite this: *Chem. Sci.*, 2025, **16**, 18372

All publication charges for this article have been paid for by the Royal Society of Chemistry

Received 14th June 2025
Accepted 26th August 2025

DOI: 10.1039/d5sc04375a

rsc.li/chemical-science

Potential-driven dynamic strain in chemical bonds for urea electrosynthesis

Xin Zhang,†[a] Hao Sun,†[a] Hai-Yan Zheng,[b] Zhan Shi,[a] Jian-Rong Zeng,[cd] Jing-Yao Liu,*[a] Chun-Yi Sun*[b] and Zhong-Min Su*[a]

Regulating the bond lengths of electrocatalysts to manipulate their surface-attached intermediates is crucial for orienting the parallel NO_3^- and CO_2 reduction pathways towards the target urea product. However, in potentiostatic systems, the fixed bond lengths cannot selectively control the competition among multiple thermodynamic processes. Herein, we successfully balanced the activities of NO_3^- and CO_2 reduction in urea electrosynthesis by constructing a potential-driven dynamic system, in which the Cu–O bond lengths in the Cu_5-PPF electrocatalyst were precisely controlled between 2.12/2.24 Å and 2.37/2.34 Å. The dynamic elastic strain of Cu–O bond lengths optimized the N- and C-pathways separately, achieving the highest urea-selective performance at equilibrium. In the dynamic system, the FE_{urea} was up to 61.6%. *In situ* spectroscopy and theoretical analyses revealed that the shorter Cu–O bond lengths favored the N-pathway, promoting the generation of key *NO intermediates, while the elongated Cu–O bond lengths enhanced the adsorption of CO_2 and the formation of *COOH in the C-pathway. Moreover, controlled experiments revealed that the dynamic system did not enhance the FE_{urea} of Cu_3-TPF and Cu_3-clusters due to their structural rigidity, further highlighting the importance of dynamic bond strain in optimizing catalytic performance.

Introduction

Electrosynthesis of urea offers a sustainable alternative to the conventional Bosch–Meiser process, helping to alleviate the energy crisis.[1–3] However, the selectivity of urea is usually undesirable due to the competition among complex thermodynamic pathways.[4–6] To overcome the thermodynamic energy barrier of the critical C–N coupling step, significant efforts have focused on developing novel catalysts, as outlined in Table S1.[7–10] Despite these advancements, optimizing the C–N coupling step alone is insufficient to enhance the urea selectivity throughout the entire reaction sequence. The competition from parallel reduction reactions, specifically the NO_3^- reduction reaction (NO_3RR) and CO_2 reduction reaction (CO_2RR), severely impedes urea formation.[11,12] In general, the rate determining step requires the selective progression of the NO_3RR and CO_2RR to a certain stage, producing specific C-species and N-species to form C–N bonds. However, in most cases, undesired side reactions always outweigh urea formation due to the overwhelming reduction of one reactant over the other.[13–15] For example, the C-pathway often generates by-products such as CO, CH_4, HCOOH and C_2H_4,[16–21] while the N-pathway produces unwanted species like NO_2^-, NO, N_2, N_2H_4, and NH_4^+.[22,23] Therefore, developing strategies to finely manipulate the competition among these reactions in urea electrosynthesis is essential but remains a significant challenge.

The selectivity and conversion rate of urea electrosynthesis benefit from precise control over the activities of parallel NO_3^- and CO_2 reductions.[24,25] Regulating the bond lengths of electrocatalysts to manipulate their surface-attached intermediates is a promising strategy for orienting multiple thermodynamic pathways towards the target product.[26,27] The length of the metal–ligand bond (M–L bond) is an intrinsic property of the electrocatalyst that affects electron distribution, polarity, and the energy gap.[28–32] Numerous studies have shown that adjusting M–L bond lengths can influence the adsorption behavior and binding energy of active species.[33–36] For example, Qin's team showed that incorporating Sb into CuS elongated the Cu–S bond from 2.24 Å to 2.30 Å, which shifted the CO_2RR product selectivity from HCOOH to CO by modulating the binding mode of intermediates.[37] Wang's team demonstrated that extending the Cu–O bond length in the Cu_1–CeO_2 catalyst induced the formation of hindered Lewis pairs, facilitating the

[a]*State Key Laboratory of Supramolecular Structure and Materials, Institute of Theoretical Chemistry, College of Chemistry, Jilin University, Changchun, Jilin, 130024, China. E-mail: ljy121@jlu.edu.cn; suzhongmin@jlu.edu.cn*

[b]*Key Laboratory of Polyoxometalate and Reticular Material Chemistry of Ministry of Education, Department of Chemistry, Northeast Normal University, Changchun, Jilin, 130024, China. E-mail: suncy009@nenu.edu.cn*

[c]*Shanghai Synchrotron Radiation Facility, Shanghai Advanced Research Institute, Chinese Academy of Sciences, 201204 Shanghai, P. R. China*

[d]*Shanghai Institute of Applied Physics, Chinese Academy of Sciences, 201800 Shanghai, P. R. China*

† These authors contributed equally to this work.

effective activation of CO_2.[5] In contrast, shorter bond lengths appear to be more favorable in the NO_3RR. Zhu *et al.* showed that hcp-Ru_1Co catalysts with shorter Ru–Co bond lengths exhibited enhanced NO_3^- adsorption. Furthermore, the strengthened interatomic interactions between Ru and Co at shorter bond lengths effectively lowered the free energy barriers for the hydrogenation of key *NO intermediates.[38] Although significant achievements have been made in exploring the relationship between bond lengths and reaction mechanisms, optimizing multiple competing sequential steps simultaneously throughout the sequential reaction is still difficult in static systems.

In this work, we constructed a dynamic system to separately optimize the C- and N-pathways in urea synthesis by precisely controlling the bond lengths of the electrocatalyst. We used a $Cu_5Cl_2(\mu_3\text{-}OH)_2$ pentacluster-based porous honeycomb-like 3D framework ($Cu_5Cl_2(\mu_3\text{-}OH)_2$ PPF) as the initial structure, which was subsequently dechlorinated and deoxygenated under operating conditions to generate Cu_5-PPF as the catalyst. Experimental and theoretical evidence suggested when the pulse potential alternated between −0.5 V and −0.7 V (*vs.* RHE), the Cu–O bond lengths in Cu_5-PPF dynamically switched between 2.12/2.24 Å and 2.37/2.34 Å. The elastic strain of the Cu–O bonds kept the catalytic center in an 'alternating activated' state, dynamically regulating the surface-bonded N- and C-intermediates. The shorter Cu–O bond length at −0.5 V favored the formation of the critical *NO species in the N-pathway, whereas the elongated Cu–O bond length at −0.7 V promoted CO_2 adsorption and the formation of *COOH in the C-pathway. The periodic elastic strain of the bond lengths alternated between the dominance of the N- and C-pathways, directing the entire reaction sequence towards the desired urea product. Compared to potentiostatic conditions (FE_{urea} = 33.1%), the dynamic system achieved a remarkable increase in FE_{urea} to 61.6%. To further assess the role of strain effects on bond length, we selected Cu_3-TPF and Cu_3-clusters as comparative samples and evaluated their electrocatalytic performance. Unfortunately, these systems did not exhibit an improved FE_{urea} under pulse-driven dynamic conditions, likely due to the structural rigidity of the triangular Cu_3-coordinated pattern. This work deepens the understanding of the structure–activity relationship and offers a novel approach to control the competitive electrocatalytic pathways in dynamic systems.

Results and discussion

Preparation and characterization of the electrocatalyst

$Cu_5Cl_2(\mu_3\text{-}OH)_2$ PPF was synthesized based on a report from Huang's group.[39] The structure of $Cu_5Cl_2(\mu_3\text{-}OH)_2$ PPF is depicted in Fig. 1a. In $Cu_5Cl_2(\mu_3\text{-}OH)_2$ PPF, two triangular clusters of $[Cu_3(\mu_3\text{-}OH)]^{4+}$ are linked together by a shared center Cu to form a square $[Cu_5(\mu_3\text{-}OH)_2(btca)_4]^-$ pentacene cluster. Each $[Cu_5(\mu_3\text{-}OH)_2(btca)_4]^-$ pentacluster was connected to ten identical pentacluster nodes *via* benzotriazole-5-carboxylic acid ligands (H_2btca) to generate a three-dimensional metal–organic framework with 1D channels. The scanning electron microscopy (SEM) and powder X-ray diffraction (PXRD) patterns of $Cu_5Cl_2(\mu_3\text{-}OH)_2$ PPF are displayed in Fig. 1b and c, respectively. All coordinated Cu atoms in $Cu_5Cl_2(\mu_3\text{-}OH)_2$ PPF were in the Cu(II) oxidation state (Fig. 1d and e).

Potential-driven elastic strain of chemical bonds for electrocatalytic urea synthesis

According to previous reports, the coordination pattern of μ_3-O in tricopper can be disrupted under electrolysis conditions.[40] To determine the reliable structure of active sites, we calculated the energy changes for dechlorination (−0.08 eV) and dehydroxylation (−0.39 eV) of $Cu_5Cl_2(\mu_3\text{-}OH)_2$ PPF, as illustrated in Fig. 2a. The results indicated that these processes were feasible under working conditions. Cyclic voltammetry of $Cu_5Cl_2(\mu_3\text{-}OH)_2$ PPF further confirmed the removal of chlorine and hydroxyl groups. As shown in Fig. S1, a clear reduction peak was observed, indicating that the structural transformation was electrochemically irreversible. Consequently, Cu_5-PPF was identified as the active structure for urea electrosynthesis.

The electrochemical performance of Cu_5-PPF for the CO_2RR, NO_3RR and CO_2/NO_3^- co-reduction was determined in neutral media. The corresponding linear sweep voltammetry (LSV) curves in Fig. 2b indicated that under CO_2/NO_3^- co-reduction conditions, Cu_5-PPF exhibited higher activity than in the CO_2RR and NO_3RR at each potential, suggesting an additional current density generated by C–N coupling.[4,41] Isotope labeling experiments confirmed the formation of $^{14}NH_2CO^{14}NH_2$ and $^{15}NH_2\text{-}CO^{15}NH_2$ products (Fig. 2c). High performance liquid chromatography (HPLC) and colorimetric methods were utilized to quantify the urea product (Fig. 2d, S2 and S3). Additionally, the content of NH_4^+ and NO_2^- was determined by the indophenol blue method and naphthalenediamine hydrochloride method, respectively (Fig. S4 and S5).

Fig. 2e shows the trend of FE_{urea} with potential for Cu_5-PPF under potentiostatic conditions. Notably, we observed two optimal FE_{urea} at −0.5 V and −0.7 V, respectively, which were atypical compared to conventional volcano plots with only a single peak. Following this discovery, we assessed the CO_2RR and NO_3RR performance of Cu_5-PPF (Fig. S6). As the applied potential shifted negatively, the products of the CO_2RR transitioned from a predominance of H_2 to carbon-based products. In the case of the NO_3RR, the primary product NO_2^- at lower potential was gradually supplanted by NH_4^+ at higher potentials. NH_4^+ is the final product of NO_3^- reduction, and its formation severely competes with the C–N coupling pathway.[6,8,25,42] For efficient urea generation, the incomplete reduction of the C- and N-pathways is superior because it enables the accumulation of specific intermediates that play crucial roles in urea production.[43,44] Consequently, we speculated that there were two optimal potentials of −0.5 V and −0.7 V in our system, corresponding to the N- and C-pathways, respectively. Less NH_4^+ was generated at −0.5 V, facilitating the production of massive incompletely reduced intermediates that were essential for the subsequent C–N coupling step. Additionally, significant conversion of CO_2 was observed as the applied potential shifted negatively from −0.7 V, initiating the sufficient activation of the C-pathway. This analysis provided

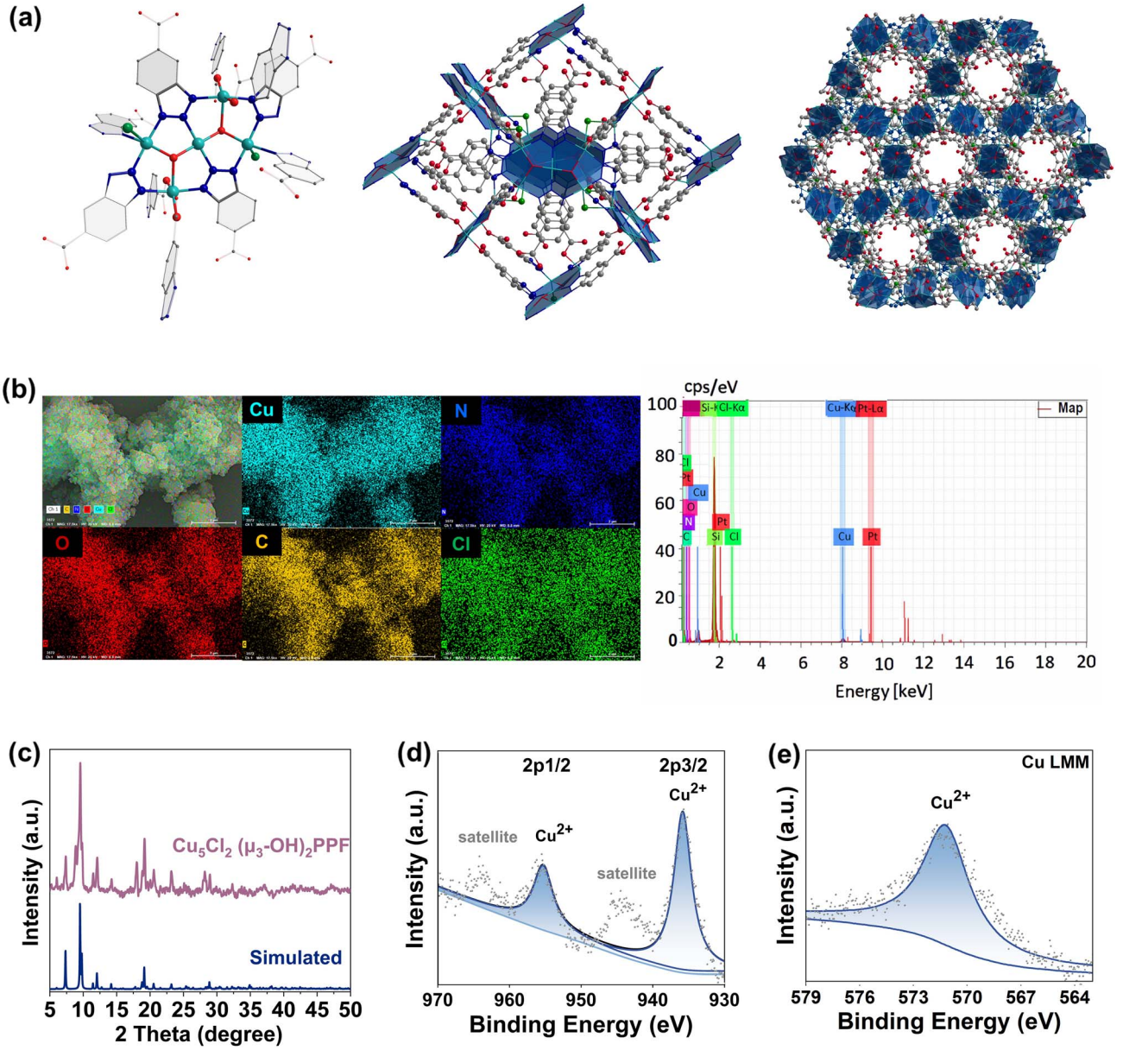

Fig. 1 (a) From left to right, the secondary building unit, ligand linking mode and 1-dimensional cavity channel of $Cu_5Cl_2(\mu_3\text{-}OH)_2$ PPF. Among them, cyan, blue, gray, red, and green represent Cu, N, C, O, and Cl atoms, respectively. (b) SEM morphology and SEM-EDS mapping images of $Cu_5Cl_2(\mu_3\text{-}OH)_2$ PPF. (c) PXRD and (d) XPS patterns and (e) Cu LMM Auger spectrum of $Cu_5Cl_2(\mu_3\text{-}OH)_2$ PPF.

insights into the two FE_{urea} peaks observed at −0.5 V and −0.7 V.

We delve into the intrinsic mechanism of modulation driven by −0.5 V and −0.7 V from the unique structure of Cu_5-PPF. As shown in Fig. 2a, although Cu_5-PPF retained a similar framework to that of $Cu_5Cl_2(\mu_3\text{-}OH)_2$ PPF, the removal of coordinated Cl and μ_3-OH groups introduces flexibility into the tetragonal $[Cu_5]^-$ pentacluster backbone. Studies have shown that increased applied voltage can lead to the elongation of bond lengths.[45,46] To investigate this, we calculated the bond lengths of Cu_5-PPF under applied potentials of −0.5 V and −0.7 V employing constant-potential DFT, in which the electrode potential was simulated by tuning the system's work function through adjusting the total number of electrons. This approach, which has been widely used for modeling electrochemical interfaces,[43,47,48] enables the assessment of how applied potential modulates electron transfer between Cu and N/O atoms, thereby influencing bond orders and resulting in bond length variations. As depicted in Fig. 2h, the Cu–O bond lengths in Cu_5-PPF extended from 2.12/2.24 Å at −0.5 V to 2.37/2.34 Å at −0.7 V. The average bond length of the chemical bonds coordinated to Cu sites extended from 1.94 Å at −0.5 V to 1.96 Å at −0.7 V. According to previous studies, the length of the M–L coordination bond significantly affects the selectivity of electrocatalytic reactions.[5,49,50] In particular, two distinct bond lengths can direct completely different CO_2RR pathways in the same

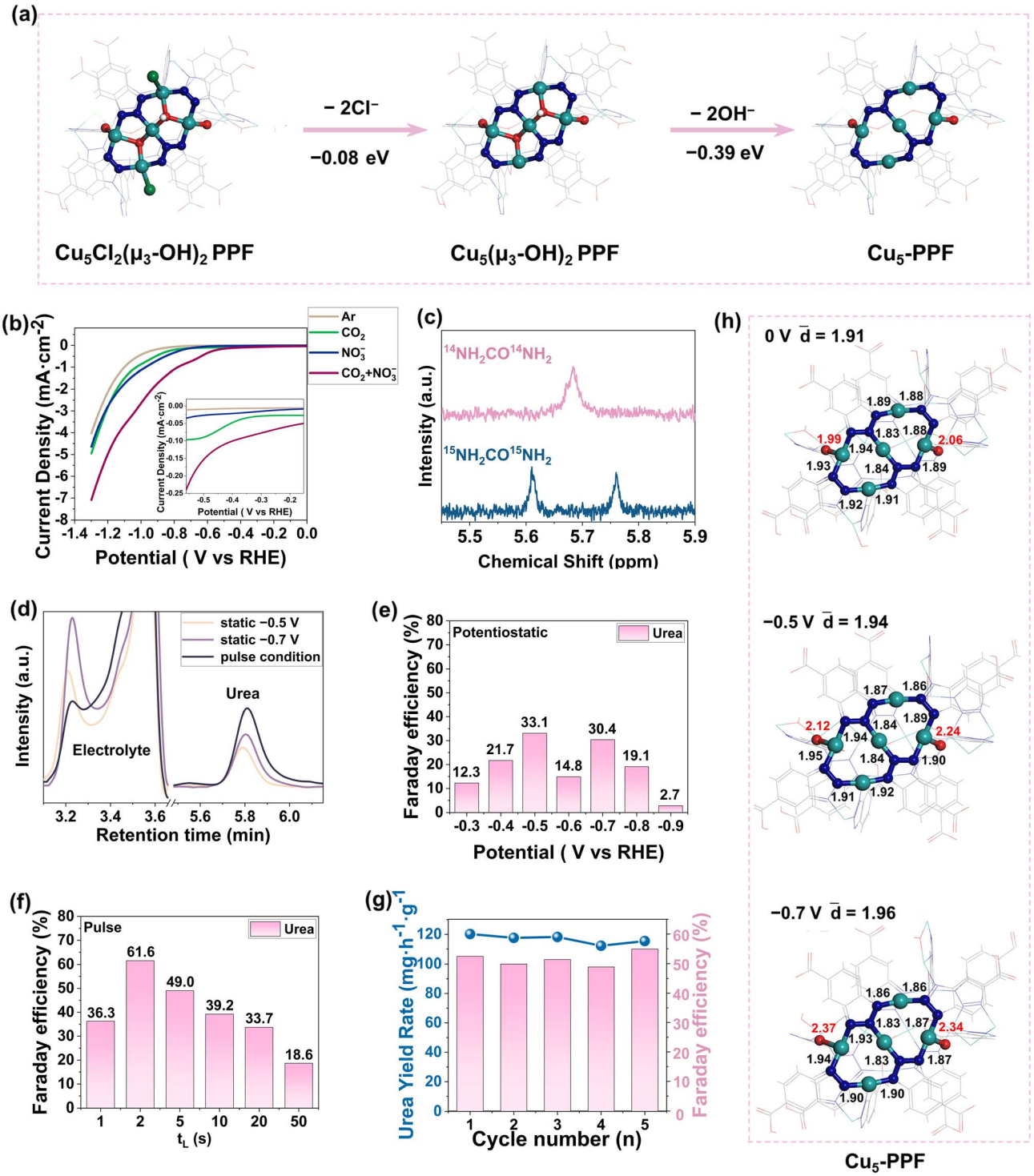

Fig. 2 (a) Energy changes of dechlorination and dehydroxylation for $Cu_5Cl_2(\mu_3\text{-}OH)_2$ PPF. (b) LSV curve for Cu_5-PPF under different conditions. (c) ^{1}H-NMR spectrum of $^{14}NH_2CO^{14}NH_2$ and $^{15}NH_2CO^{15}NH_2$. (d) HPLC spectra of urea generated from potentiostatic conditions and pulsed conditions. (e) FE_{urea} on Cu_5-PPF under potentiostatic conditions. (f) Variation of FE_{urea} with t_L under pulsed conditions. Here, the t_U was set to 10 s, and the E_U and E_L were set to −0.5 V (*vs.* RHE) and −0.7 V (*vs.* RHE), respectively. All the C–N coupling reactions were carried out in 8 mM KNO_3 + 0.2 M K_2SO_4 solution saturated with CO_2. (g) $Yield_{urea}$ and FE_{urea} for 5 cycles on Cu_5-PPF. (h) Calculated bond lengths near the Cu sites of Cu_5-PPF at applied potentials of 0 V, −0.5 V, and −0.7 V, respectively.

reaction system.[37] For Cu_5-PPF, the bond length states induced by −0.5 V and −0.7 V likely manipulate two reaction pathways, specifically the corresponding N- and C-pathways.

By applying the pulse procedure with −0.5 V as the upper limit cathode potential (E_U) and −0.7 V as the lower limit cathode potential (E_L), dynamic elastic strain of the bond

lengths was induced by the alternating potentials. The impact of this dynamic system on urea performance is shown in Fig. 2f and S7, where the durations of upper limit cathode potential (t_U) and lower limit cathode potential (t_L) were optimized. Under optimal conditions of $t_U = 10$ s and $t_L = 2$ s, the FE_{urea} reached up to 61.6%. We further investigated the effect of the pulse potential direction by fixing the onset potential at −0.5 V. As shown in Fig. S8, applying more negative pulse potentials favored the urea formation pathway compared to less negative pulses. Notably, even when the less negative potential in the cycle is above the onset potential, urea is produced during the −0.5 V interval and contributes to the cycle-averaged FE. Under pulsed conditions, the overall product distribution is determined by the full time-dependent sequence rather than by any instantaneous potential alone. Compared to the highest urea formation rate ($Yield_{urea}$) under potentiostatic conditions (65.06 mg h^{-1} g^{-1}), the dynamic system enhanced the $Yield_{urea}$ to 110.41 mg h^{-1} g^{-1} (Fig. S9). The dynamic bond length strain facilitated the sequential dominance of the C- and N-pathways within the same system, ultimately achieving the highest urea performance at optimal equilibrium. As depicted in Fig. 2g, the catalytic ability of Cu_5-PPF was maintained after 5 catalytic cycles. Moreover, Cu_5-PPF was able to operate for 3300 pulse cycles (shown in Fig. S10). The CO_2RR and NO_3RR performance

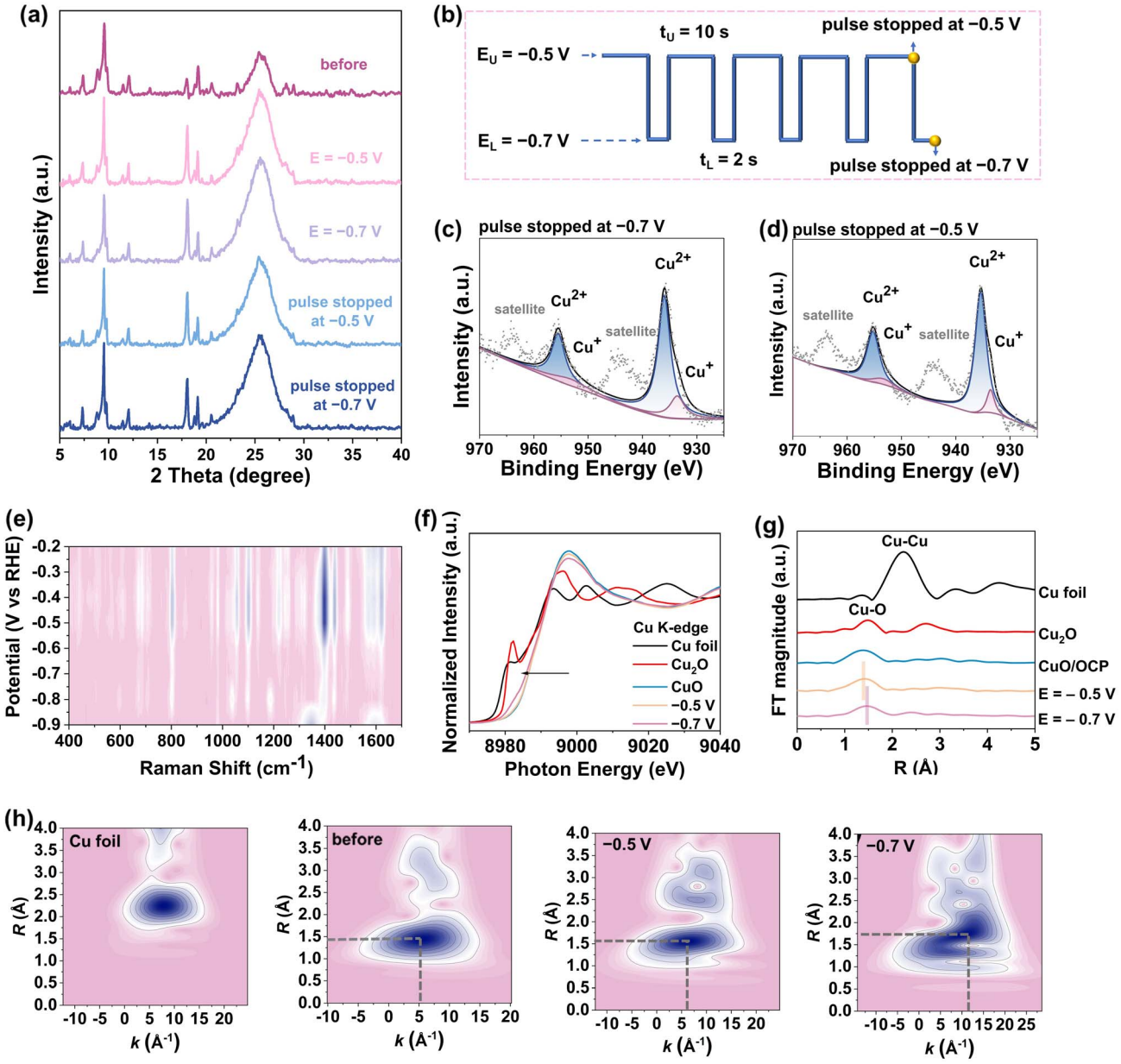

Fig. 3 (a) PXRD comparison of Cu_5-PPF before and after 2 h of electrolysis. (b) Schematic diagram for the pulse sequence stopped at −0.5 V and −0.7 V. XPS spectra of Cu_5-PPF after 2 h of electrolysis under pulsed conditions with the potential sequence stopped at (c) −0.7 V and (d) −0.5 V. (e) *In situ* Raman spectra of Cu_5-PPF. (f) Cu K-edge XANES and (g) FT-EXAFS spectra of Cu_5-PPF. (h) Wavelet-transform plots of Cu foil, $Cu_5Cl_2(\mu_3\text{-}OH)_2$ PPF, and Cu_5-PPF at −0.5 V and −0.7 V, respectively.

of Cu_5-PPF under pulsed conditions is presented in Fig. S11, emphasizing the incomplete reduction of C- and N-pathways that favored C–N coupling.

Fig. S12 and S13 illustrate the morphology and elemental distribution of Cu_5-PPF after the electrolysis reaction, demonstrating a uniform distribution of Cu, N, O, and C elements. In contrast, the Cl element showed a significant dissociation compared to the initial $Cu_5Cl_2(\mu_3\text{-}OH)_2$ PPF, which aligned with the theoretical analysis. Fig. 3b presents a schematic representation indicating the termination position of the pulse sequence after 2 hours of electrolysis. As shown in Fig. 3a, the crystalline phase of Cu_5-PPF essentially preserved the original characteristics under both static and pulsed electrolysis. X-ray photoelectron spectroscopy (XPS) analysis revealed that the valence of Cu remained unchanged with varying pulse potentials, suggesting that the Cu oxidation states did not serve as an intrinsic character contributing to the dynamic modulation (Fig. 3c, d and S14). The Cu K-edge XANES spectra indicated that the Cu valence in Cu_5-PPF ranged between +1 and +2 under working conditions, attributed to the removal of Cl and μ_3-OH groups (Fig. 3f). *In situ* Raman spectroscopy was conducted to evaluate the electrochemical stability of Cu_5-PPF under varying applied potentials. As illustrated in Fig. 3e, Cu_5-PPF maintained its structural integrity at low potentials up to −0.7 V. Beyond this threshold, the intensity of characteristic vibrational signals declined markedly, and new peaks emerged at 1035 and 1188 cm^{-1}, indicating the formation of new chemical bonds. At −0.9 V, the original Cu_5-PPF framework was fully disrupted. Accordingly, −0.7 V was identified as the critical potential for structural preservation. At more negative potentials, excessive bond elongation led to bond cleavage and the formation of new bonding configurations. Fourier transform extended X-ray absorption fine structure (FT-EXAFS) and wavelet transform (WT)-EXAFS analysis of the Cu K-edge corroborated the significant elongation of the Cu–O/N bond at −0.7 V in comparison to both −0.5 V and the standard sample (Fig. 3g and h). Cu K-edge EXAFS fitting curves and the parameters for the Cu–N/O bonds in *R* space are displayed in Fig. S15 and Table S2. Compared to the original structure, the average Cu–N/O bond lengths extended to 1.93 Å and 1.95 Å at −0.5 V and −0.7 V, respectively. These experimental results validated the potential-induced elastic strain in the chemical bonds of Cu_5-PPF, thereby enabling the catalyst to flexibly adjust and adapt to the adsorption of various intermediates under pulse sequences.

Dynamic strain effect of bond lengths on reaction pathways

Advanced *in situ* attenuated total reflectance Fourier transform infrared spectroscopy (ATR-FTIR) was employed to monitor the evolution of reaction intermediates on Cu_5-PPF during urea generation. As shown in Fig. 4a, the peak at 1456 cm^{-1} was assigned to the formation of the C–N bond, indicating successful urea synthesis. A distinct band at 1215 cm^{-1} was attributed to the *COOH intermediate. Additionally, signals corresponding to $*NO_2$, *NO and $*NH_2$ species were detected, confirming the stepwise reduction of NO_3^-. Notably, the *OCNO intermediate was identified by a characteristic peak at 2066 cm^{-1}, providing key mechanistic insight into the urea formation pathway.

Guided by these ATR-FTIR findings, Density Functional Theory (DFT) calculations were subsequently performed to elucidate the detailed reaction mechanisms. Although constant-potential DFT cannot capture the full dynamic evolution of metastable catalyst states during pulsed electrolysis, analyzing reaction pathways at representative static potentials (*e.g.*, −0.5 V and −0.7 V) has been widely adopted to gain qualitative insight into pulse-driven mechanisms and is considered a practical and informative approximation under current computational limitations.[51–54] These two potentials are not intended to mimic real-time oscillation, but rather to approximate the anodic and cathodic conditions within the pulse cycle. Researchers have indicated that the length of M–L significantly affected the adsorption properties of active intermediates, further controlling the reaction pathways.[55,56] To delve deeper into the impact of the elastic strain of bond lengths on the reaction, we calculated the Gibbs free energy profiles on Cu_5-PPF at −0.5 V and −0.7 V (Tables S3 and S4). In our system, the key N- and C-species for the first step of C–N coupling were *NO and *COOH, respectively. For the N-pathway shown in Fig. 4b, free energy changes (ΔG) for all *NO intermediate formation steps at −0.5 V were lower than the corresponding steps at −0.7 V, indicating a preference for shorter bond lengths in N-containing species generation. Electrostatic potential analysis revealed that the catalyst surface exhibited more positive potential regions at −0.5 V, facilitating preferential adsorption of negatively charged NO_3^- (Fig. S16). For the initial step in the N-pathway ($*NO_3 \rightarrow *HNO_3$), hydrogenation at −0.5 V was energetically more favorable than that at −0.7 V, which can be attributed to differences in the adsorption configurations of $*NO_3$. Several $*NO_3$ adsorption modes were considered, including single O-bonding to edge or central Cu–N sites, double O-bonding involving two edge Cu–N sites, and double O-bonding to edge Cu and central Cu–N/O sites. A potential-dependent trend was observed: at −0.5 V, double O-bonding configurations were preferred, promoting $*NO_3$ activation and subsequent hydrogenation, whereas at −0.7 V, single O-bonding became more stable (Fig. S17). Similar site-specific bonding behavior and Cu-site synergy were also observed for other key intermediates along the reaction pathway. The second rate-determining step of the N-pathway was governed by the elastic strain of the Cu–O bonds in Cu_5-PPF. Elongation of the Cu–O bond lengths at higher potentials enabled the Cu atoms to carry more positive charge, enhancing the binding with the oxygen atom in $*NO_2$ and making the subsequent ring-opening hydrogenation more difficult. Consequently, the shorter Cu–O bond lengths driven by −0.5 V resulted in a lower energy change for the $*NO_2 \rightarrow *HNO_2$ step. Additionally, the shorter Cu–O bond length was more favorable for both the first and second C–N coupling steps (Fig. 4c and d). Calculations depicted in Fig. 4d revealed that for the C-pathway, a more negative potential (−0.7 V) favored the formation of C-containing intermediates. The extended Cu–O bond lengths driven by −0.7 V allowed the Cu atoms with more positive charge to stabilize the O-terminus of $*CO_2$, promoting adsorption of CO_2 and *COOH formation with thermodynamically supported ΔG values of −0.58 eV and −0.16 eV compared to 0.12 eV and −0.02 eV at −0.5 V.

In summary, the significant elastic strain of bond lengths in Cu_5-PPF regulated the adsorption strength and the binding

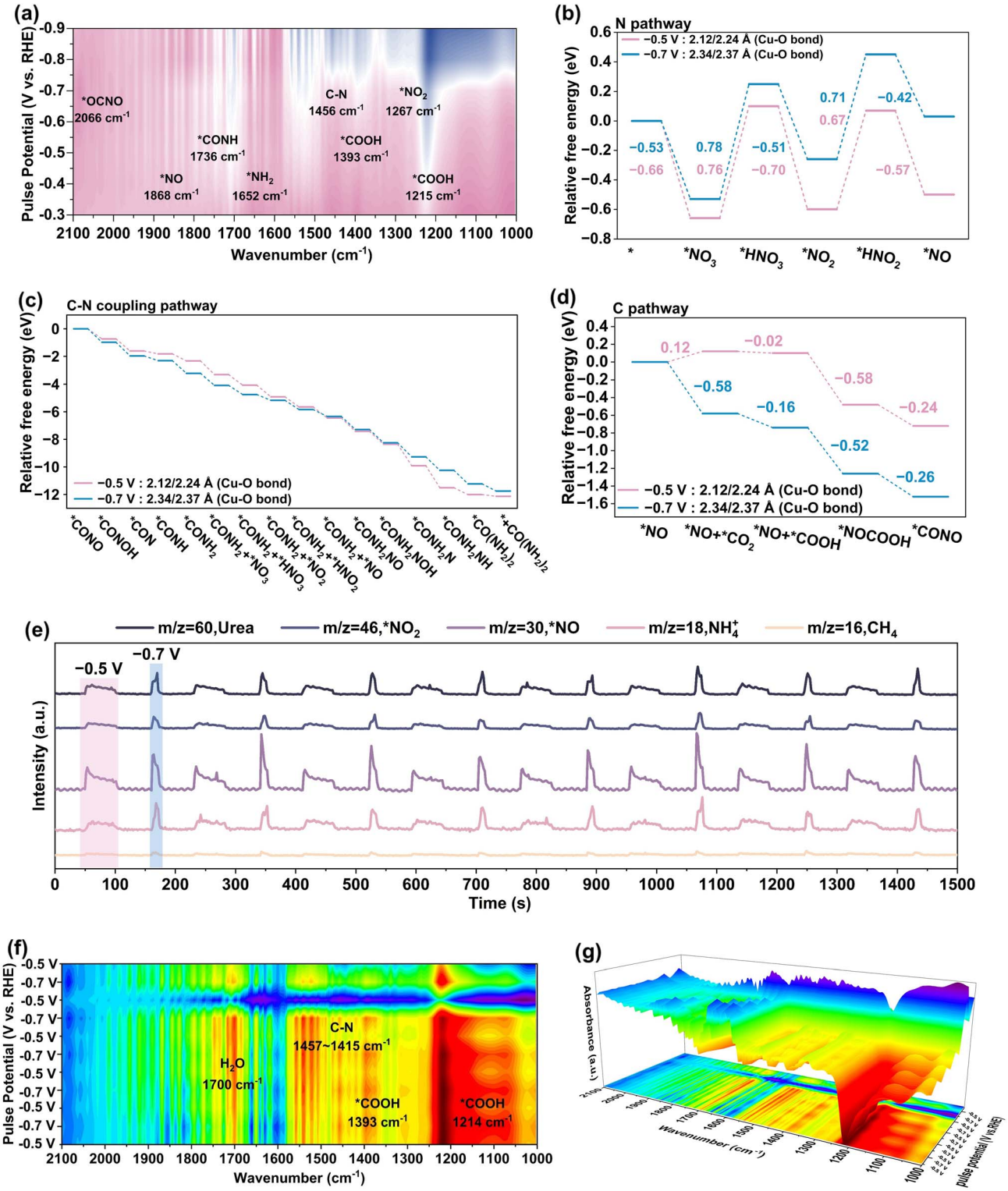

Fig. 4 (a) ATR-FTIR measurements under various potentials for Cu_5-PPF. Free energy profiles of (b) N-containing intermediates, (c) C–N coupling, and (d) C-containing intermediate pathways during urea electrosynthesis on Cu_5-PPF at −0.5 V and −0.7 V. (e) DEMS measurements of Cu_5-PPF during urea production. In CO_2 saturated 8 mM KNO_3 + 0.2 M K_2SO_4 solution, signals at $m/z = 60$ (urea), $m/z = 46$ (*NO_2), $m/z = 30$ (*NO), $m/z = 18$ (NH_4^+) and $m/z = 16$ (CH_4) were recorded simultaneously. The tested potential pulse consists of a cathodic period at −0.5 V for 50 s and a period at −0.7 V for 10 s. Each individual electrolysis reaction was followed by a power-off period of 60 s to flush out air bubbles left in the chamber from the previous test. (f) ATR-FTIR and (g) the corresponding three-dimensional spectra of Cu_5-PPF under pulsed cycling.

behavior of intermediates. The elongated bond lengths induced by −0.7 V favored the adsorption of CO_2 and formation of *COOH intermediates, but tended to generate large amounts of NH_4^+ by-product. Conversely, shorter bond lengths driven by −0.5 V facilitated the production of essential *NO species but struggled to adsorb sufficient CO_2 for C–N coupling, in agreement with the experimental results depicted in Fig. S18. By precisely controlling the elastic strain of bond lengths through periodic alternating potentials, a dynamic switch between optimal N- and C-pathways within the same catalytic system was achieved.

Combined with theoretical calculations, we identified *COOH and *NO as the key intermediates in the C–N coupling pathway. *In situ* differential electrochemical mass spectroscopy (DEMS) was employed to monitor intermediates at −0.5 V and −0.7 V (Fig. 4e). Due to the continuous CO_2 flow during the experiment, direct detection of CO_2 signals was not feasible. Instead, CH_4, a reduction product of *COOH, was used as a marker of the C pathway.[57] No CH_4 signal was observed at −0.5 V, while a weak CH_4 signal emerged at −0.7 V, suggesting that the elongated Cu–O bonds at −0.7 V facilitated CO_2 adsorption and activation, in agreement with DFT results. For the N pathway, the *NO intermediate showed a strong signal relative to NO_2^- and NH_4^+, confirming its key role in urea production. These *in situ* DEMS results validated the formation of *COOH and *NO intermediates, thereby supporting the proposed reaction mechanism. Moreover, DEMS measurements under alternating potentials (−0.5 V and −0.7 V) further confirmed the dynamic evolution of active intermediates.

The ATR-FTIR spectra under dynamic conditions further demonstrated the response of the intermediates to the pulse potential, as shown in Fig. 4f and g. As the Cu–O bond lengths underwent dynamic strain, a clear periodic fluctuation in the strength of the C–N bonds and *COOH intermediates was observed. Notably, the formation of *COOH intermediates was preferentially favored in the extended bond length state, consistent with the free energy change and *in situ* DEMS analysis. As the pulse cycle progressed, the peak intensity at 1700 cm^{-1} decreased due to the constant consumption of H_2O. The consumption and dissociation of H_2O generated a large amount of *H, which actively participated in the catalytic reaction to form intermediates.[58,59]

Electrocatalytic performance of rigid structures under dynamic conditions

To further explore the dynamic elastic strain of bond lengths on urea electrosynthesis, we selected a trinuclear cluster-based porous tubular 3D framework ($Cu_3\mu_3$-O TPF) and $Cu_3\mu_3$-OH trinuclear clusters ($Cu_3\mu_3$-OH clusters) as comparison structures. The energy calculations for deoxidation of $Cu_3\mu_3$-O TPF and dehydroxylation of $Cu_3\mu_3$-OH clusters are shown in Fig. 5a and b, respectively. We identified Cu_3-TPF and Cu_3-clusters as the active structure under working conditions. The XRD pattern, XPS and

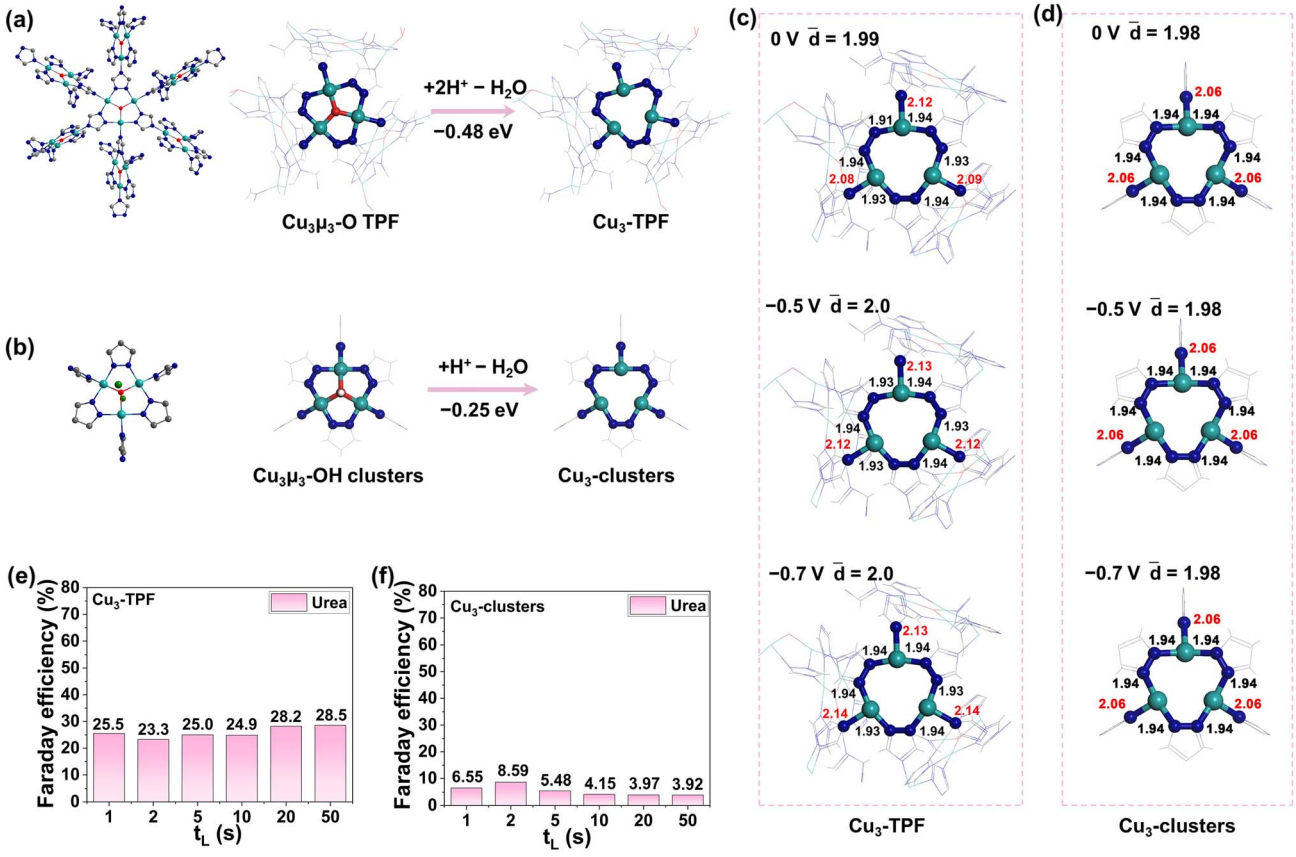

Fig. 5 Energy changes of (a) deoxidization for $Cu_3\mu_3$-O TPF and (b) dihydroxylation for $Cu_3\mu_3$-OH. Bond lengths near the Cu sites of (c) Cu_3-TPF and (d) Cu_3-clusters at applied potentials of 0 V, −0.5 V, and −0.7 V, respectively. Variation of FE_{urea} with t_L under pulsed conditions for (e) Cu_3-TPF and (f) Cu_3-clusters. The electrocatalytic conditions were consistent with those of Cu_5-PPF.

Cu LMM spectra of Cu_3-TPF and Cu_3-clusters are presented in Fig. S19–S22. The 3D structure and 1D channels of $Cu_3\mu_3$-O TPF are depicted in Fig. S23. *In situ* Raman was employed to monitor the structural evolution of Cu_3-TPF at different potentials. As shown in Fig. S24, Cu_3-TPF exhibited pronounced stability. Though some new chemical bonds emerged within the 1100 to 2000 cm^{-1} range at −0.9 V, the primary framework remained intact. We calculated the variations in bond lengths around the Cu sites of Cu_3-TPF at −0.5 V and −0.7 V. Compared to Cu_5-PPF, the average bond lengths of Cu_3-TPF exhibited minor changes (Fig. 5c), likely due to the more rigid planar triangular coordination mode of Cu_3 compared to the distorted square coordination of Cu_5-PPF. For Cu_3-TPF, the pulsed conditions did not enhance the urea selectivity, but instead resulted in a decrease compared to potentiostatic electrolysis (Fig. 5e and S25). This could be attributed to the inadequate strain of bond lengths in Cu_3-TPF to effectively modulate the C- and N-pathways. The situation for Cu_3-clusters was similar to that of Cu_3-TPF. Moreover, the urea synthesis activity of Cu_3-clusters was even less favorable due to their more rigid structure (Fig. 5d and f). The $Yield_{urea}$ values of Cu_3-TPF and Cu_3-clusters are shown in Fig. S26 and S27, which were much lower than that of Cu_5-PPF under the same conditions. These results demonstrated the importance of dynamically evolving bond lengths in urea production.

Conclusion

In this work, we presented an effective strategy to control the parallel NO_3RR and CO_2RR pathways toward the desired urea product by dynamically regulating the elastic strain in the Cu–O bonds. The well-defined $Cu_5Cl_2(\mu_3\text{-}OH)_2$ PPF served as the initial structure, which was subsequently dechlorinated and deoxygenated under working conditions to form Cu_5-PPF as the catalyst. Benefiting from the structural flexibility of Cu_5-PPF, dynamic elastic strain in the Cu–O bond lengths was induced by pulsed potentials. *In situ* spectroscopy combined with DFT results confirmed that the shorter Cu–O bond lengths driven by −0.5 V dominated the formation of key *NO species in the N-pathway. Furthermore, the elongation of Cu–O bonds promoted the adsorption of CO_2 and the formation of *COOH intermediates in the C-pathway. The dynamic strain effect on Cu–O bond lengths optimized the N- and C-pathways separately, ultimately reaching an equilibrium point of the highest urea selectivity. Under dynamic conditions, the FE_{urea} was up to 61.6%. To further validate the importance of the strain effect on bond lengths, we evaluated the rigidly structured Cu_3-TPF and Cu_3-clusters and assessed their urea synthesis performance. Since the bond lengths of Cu_3-TPF and Cu_3-clusters exhibited minimal strain, the pulse-driven dynamic system did not enhance their FE_{urea}. Our work provides valuable insights into the structure–activity relationship and inspires new directions for regulating multiple reaction pathways in dynamic systems.

Author contributions

Xin Zhang carried out the experimental studies: synthesis, characterization, catalysis and data analysis. Hao Sun carried out the computational studies. Hai-Yan Zheng and Jian-Rong Zeng carried out the XAS experiments. Jing-Yao Liu, Chun-Yi Sun, Zhan Shi, and Zhong-Min Su supervised the whole project. All authors contributed to the writing of this manuscript and they have given approval to the final version of the manuscript.

Conflicts of interest

There are no conflicts to declare.

Data availability

The data supporting this article have been included as a part of the SI. See DOI: **https://doi.org/10.1039/d5sc04375a**.

Acknowledgements

Xin Zhang and Hao Sun contributed equally to this work. This work was financially supported by the National Natural Science Foundation of China (21801021). We thank the staff of beamline BL13SSW at SSRF for their support during the XAS experiments.

References

1 W. Gao, Y. Xu, L. Fu, X. Chang and B. Xu, Experimental evidence of distinct sites for CO_2-to-CO and CO conversion on Cu in the electrochemical CO_2 reduction reaction, *Nat. Catal.*, 2023, **6**, 885–894.
2 P. Wei, D. Gao, T. Liu, H. Li, J. Sang, C. Wang, R. Cai, G. Wang and X. Bao, Coverage-driven selectivity switch from ethylene to acetate in high-rate CO_2/CO electrolysis, *Nat. Nanotechnol.*, 2023, **18**, 299–306.
3 M. Zheng, J. Zhang, P. Wang, H. Jin, Y. Zheng and S.-Z. Qiao, Recent Advances in Electrocatalytic Hydrogenation Reactions on Copper-Based Catalysts, *Adv. Mater.*, 2024, **36**, 2307913.
4 Q. Hu, W. Zhou, S. Qi, Q. Huo, X. Li, M. Lv, X. Chen, C. Feng, J. Yu, X. Chai, H. Yang and C. He, Pulsed co-electrolysis of carbon dioxide and nitrate for sustainable urea synthesis, *Nature Sustainability*, 2024, **7**, 442–451.
5 X. Wei, Y. Liu, X. Zhu, S. Bo, L. Xiao, C. Chen, T. T. T. Nga, Y. He, M. Qiu, C. Xie, D. Wang, Q. Liu, F. Dong, C.-L. Dong, X.-Z. Fu and S. Wang, Dynamic Reconstitution Between Copper Single Atoms and Clusters for Electrocatalytic Urea Synthesis, *Adv. Mater.*, 2023, **35**, 2300020.
6 C. Lv, L. Zhong, H. Liu, Z. Fang, C. Yan, M. Chen, Y. Kong, C. Lee, D. Liu, S. Li, J. Liu, L. Song, G. Chen, Q. Yan and G. Yu, Selective electrocatalytic synthesis of urea with nitrate and carbon dioxide, *Nature Sustainability*, 2021, **4**, 868–876.
7 W. Qiu, S. Qin, Y. Li, N. Cao, W. Cui, Z. Zhang, Z. Zhuang, D. Wang and Y. Zhang, Overcoming Electrostatic Interaction via Pulsed Electroreduction for Boosting the Electrocatalytic Urea Synthesis, *Angew. Chem., Int. Ed.*, 2024, **63**, e202402684.
8 Y. Gao, J. Wang, M. Sun, Y. Jing, L. Chen, Z. Liang, Y. Yang, C. Zhang, J. Yao and X. Wang, Tandem Catalysts Enabling

Efficient C–N Coupling toward the Electrosynthesis of Urea, *Angew. Chem., Int. Ed.*, 2024, **63**, e202402215.

9 D.-S. Huang, X.-F. Qiu, J.-R. Huang, M. Mao, L. Liu, Y. Han, Z.-H. Zhao, P.-Q. Liao and X.-M. Chen, Electrosynthesis of urea by using Fe_2O_3 nanoparticles encapsulated in a conductive metal–organic framework, *Nat. Synth.*, 2024, **3**, 1404–1413.

10 Y. Zhao, Y. Ding, W. Li, C. Liu, Y. Li, Z. Zhao, Y. Shan, F. Li, L. Sun and F. Li, Efficient urea electrosynthesis from carbon dioxide and nitrate via alternating Cu–W bimetallic C–N coupling sites, *Nat. Commun.*, 2023, **14**, 4491.

11 C. Liu, H. Tong, P. Wang, R. Huang, P. Huang, G. Zhou and L. Liu, The asymmetric orbital hybridization in single-atom-dimers for urea synthesis by optimizing the C–N coupling reaction pathway, *Appl. Catal., B*, 2023, **336**, 122917.

12 J. Qin, N. Liu, L. Chen, K. Wu, Q. Zhao, B. Liu and Z. Ye, Selective Electrochemical Urea Synthesis from Nitrate and CO_2 Using In Situ Ru Anchoring onto a Three-Dimensional Copper Electrode, *ACS Sustain. Chem. Eng.*, 2022, **10**, 15869–15875.

13 G.-F. Chen, Y. Yuan, H. Jiang, S.-Y. Ren, L.-X. Ding, L. Ma, T. Wu, J. Lu and H. Wang, Electrochemical reduction of nitrate to ammonia via direct eight-electron transfer using a copper–molecular solid catalyst, *Nat. Energy*, 2020, **5**, 605–613.

14 H. Yang, Y. Wu, G. Li, Q. Lin, Q. Hu, Q. Zhang, J. Liu and C. He, Scalable Production of Efficient Single-Atom Copper Decorated Carbon Membranes for CO_2 Electroreduction to Methanol, *J. Am. Chem. Soc.*, 2019, **141**, 12717–12723.

15 Y. Cai, J. Fu, Y. Zhou, Y.-C. Chang, Q. Min, J.-J. Zhu, Y. Lin and W. Zhu, Insights on forming N,O-coordinated Cu single-atom catalysts for electrochemical reduction CO_2 to methane, *Nat. Commun.*, 2021, **12**, 586.

16 L. Li, X. Li, Y. Sun and Y. Xie, Rational design of electrocatalytic carbon dioxide reduction for a zero-carbon network, *Chem. Soc. Rev.*, 2022, **51**, 1234–1252.

17 W. Ma, X. He, W. Wang, S. Xie, Q. Zhang and Y. Wang, Electrocatalytic reduction of CO_2 and CO to multi-carbon compounds over Cu-based catalysts, *Chem. Soc. Rev.*, 2021, **50**, 12897–12914.

18 Y. Xiao, H.-T. Zhang and M.-T. Zhang, Heterobimetallic NiFe Complex for Photocatalytic CO_2 Reduction: United Efforts of NiFe Dual Sites, *J. Am. Chem. Soc.*, 2024, **146**, 28832–28844.

19 Y. Jiang, Z. Liang, H. Fu, C. Gu and Y. Du, High-Entropy Rare Earth Oxides Anchoring Tunable $Cu^{\delta+}$ Nanochimneys for Self-Tandem C–C Coupling Catalysis, *Adv. Mater.*, 2025, **37**, 2503027.

20 Y. Jiang, H. Fu, Z. Liang, Q. Zhang and Y. Du, Rare earth oxide based electrocatalysts: synthesis, properties and applications, *Chem. Soc. Rev.*, 2024, **53**, 714–763.

21 L. Song, Z. Liang, M. Sun, B. Huang and Y. Du, The interfacial effect induced by rare earth oxide in boosting the conversion of CO_2 to formate, *Energy Environ. Sci.*, 2022, **15**, 3494–3502.

22 S. Li, X. Fu, J. K. Nørskov and I. Chorkendorff, Towards sustainable metal-mediated ammonia electrosynthesis, *Nat. Energy*, 2024, **9**, 1344–1349.

23 J. Zhang, L. Huang, W. W. Tjiu, C. Wu, M. Zhang, S. Bin Dolmanan, S. Wang, M. Wang, S. Xi, Z. Aabdin and Y. Lum, Evidence for Distinct Active Sites on Oxide-Derived Cu for Electrochemical Nitrate Reduction, *J. Am. Chem. Soc.*, 2024, **146**, 30708–30714.

24 Y. Li, S. Zheng, H. Liu, Q. Xiong, H. Yi, H. Yang, Z. Mei, Q. Zhao, Z.-W. Yin, M. Huang, Y. Lin, W. Lai, S.-X. Dou, F. Pan and S. Li, Sequential co-reduction of nitrate and carbon dioxide enables selective urea electrosynthesis, *Nat. Commun.*, 2024, **15**, 176.

25 C. Chen, S. Li, X. Zhu, S. Bo, K. Cheng, N. He, M. Qiu, C. Xie, D. Song, Y. Liu, W. Chen, Y. Li, Q. Liu, C. Li and S. Wang, Balancing sub-reaction activity to boost electrocatalytic urea synthesis using a metal-free electrocatalyst, *Carbon Energy*, 2023, **5**, e345.

26 F. He, Y. Liu, X. Yang, Y. Chen, C.-C. Yang, C.-L. Dong, Q. He, B. Yang, Z. Li, Y. Kuang, L. Lei, L. Dai and Y. Hou, Accelerating Oxygen Electrocatalysis Kinetics on Metal–Organic Frameworks via Bond Length Optimization, *Nano-Micro Lett.*, 2024, **16**, 175.

27 N. Wang, P. Ou, R. K. Miao, Y. Chang, Z. Wang, S.-F. Hung, J. Abed, A. Ozden, H.-Y. Chen, H.-L. Wu, J. E. Huang, D. Zhou, W. Ni, L. Fan, Y. Yan, T. Peng, D. Sinton, Y. Liu, H. Liang and E. H. Sargent, Doping Shortens the Metal/Metal Distance and Promotes OH Coverage in Non-Noble Acidic Oxygen Evolution Reaction Catalysts, *J. Am. Chem. Soc.*, 2023, **145**, 7829–7836.

28 J. Jiang, F. Sun, S. Zhou, W. Hu, H. Zhang, J. Dong, Z. Jiang, J. Zhao, J. Li, W. Yan and M. Wang, Atomic-level insight into super-efficient electrocatalytic oxygen evolution on iron and vanadium co-doped nickel (oxy)hydroxide, *Nat. Commun.*, 2018, **9**, 2885.

29 P. Zhang, S.-J. Ji, D. Zhang, H.-G. Xue and N.-T. Suen, Synthesis, Crystal Structure, Electronic Structure, and Electrocatalytic Hydrogen Evolution Reaction of Synthetic Perryite Mineral, *Inorg. Chem.*, 2021, **60**, 3006–3014.

30 Y. Liu, D. Wang, B. Yang, Z. Li, X. Peng, Z. Liu, L. Zeng, T. Zhang, R. D. Rodriguez, L. Lei and Y. Hou, Efficiently electrochemical CO_2 reduction on molybdenum-nitrogen-carbon catalysts with optimized p-block axial ligands, *Chem. Eng. Sci.*, 2023, **273**, 118638.

31 Y. Chen, R. Zhang, H.-T. Wang, Y.-R. Lu, Y.-C. Huang, Y.-C. Chuang, H. Wang, J. Luo and L. Han, Temperature-Dependent Structures of Single-Atom Catalysts, *Chem.–Asian J.*, 2023, **18**, e202300679.

32 J. Sun, H. Yang, W. Gao, T. Cao and G. Zhao, Diatomic Pd–Cu Metal-Phosphorus Sites for Complete N≡N Bond Formation in Photoelectrochemical Nitrate Reduction, *Angew. Chem., Int. Ed.*, 2022, **61**, e202211373.

33 C. Ye, H. Cheng, L. Zheng, J. Lin, Q. Xu, Y. Qiu, Z. Pan and Y. Qiu, Tailoring Metal–Oxygen Bonds Boosts Oxygen Reaction Kinetics for High-Performance Zinc–Air Batteries, *Nano Lett.*, 2023, **23**, 1573–1581.

34 M. Chen, Y. Zou, H. Zhao, W.-D. Zhang, Q. Gong, J. Liu, J. Wang and X. Yan, Regulating the Ni–O bond length by constructing $Ni(OH)_2$/CNTs heterostructure for enhanced

nucleophile electrocatalytic oxidation, *Chem. Eng. J.*, 2024, **497**, 154525.
35 J. Zhang, C. Guo, S. Fang, X. Zhao, L. Li, H. Jiang, Z. Liu, Z. Fan, W. Xu, J. Xiao and M. Zhong, Accelerating electrochemical CO_2 reduction to multi-carbon products via asymmetric intermediate binding at confined nanointerfaces, *Nat. Commun.*, 2023, **14**, 1298.
36 Y. Xu, Y. Zhang, H. Zhao, L. Shi, Z. Zhang, X. Li, Z. Xue, H. Jiang, Y. Zhu and J. Zhu, Optimizing the Selectivity of CH_4 Electrosynthesis from CO_2 over Cuprates through Cu–O Bond Length Descriptor, *Angew. Chem., Int. Ed.*, 2025, **64**, e202503745.
37 X. Wei, Z. Li, H. Jang, M. Gyu Kim, S. Liu, J. Cho, X. Liu and Q. Qin, Switching Product Selectivity in CO_2 Electroreduction via Cu–S Bond Length Variation, *Angew. Chem., Int. Ed.*, 2024, **63**, e202409206.
38 X. Zhu, Y.-C. Wang, K. Qu, L. Song, J. Wang, Y. Gong, X. Liu, C.-F. Li, S. Yuan, Q. Lu and A.-L. Wang, Modulating Ru-Co bond lengths in Ru_1Co single-atom alloys through crystal phase engineering for electrocatalytic nitrate-to-ammonia conversion, *Nat. Commun.*, 2025, **16**, 5742.
39 J. Xiao, B.-Y. Liu, G. Wei and X.-C. Huang, Solvent Induced Diverse Dimensional Coordination Assemblies of Cupric Benzotriazole-5-carboxylate: Syntheses, Crystal Structures, and Magnetic Properties, *Inorg. Chem.*, 2011, **50**, 11032–11038.
40 N. Li, C. Pan, G. Lu, H. Pan, Y. Han, K. Wang, P. Jin, Q. Liu and J. Jiang, Hydrophobic Trinuclear Copper Cluster-Containing Organic Framework for Synergetic Electrocatalytic Synthesis of Amino Acids, *Adv. Mater.*, 2024, **36**, 2311023.
41 X. Zhang, X. Zhu, S. Bo, C. Chen, M. Qiu, X. Wei, N. He, C. Xie, W. Chen, J. Zheng, P. Chen, S. P. Jiang, Y. Li, Q. Liu and S. Wang, Identifying and tailoring C–N coupling site for efficient urea synthesis over diatomic Fe–Ni catalyst, *Nat. Commun.*, 2022, **13**, 5337.
42 Q. Zhao, X. Lu, Y. Wang, S. Zhu, Y. Liu, F. Xiao, S. X. Dou, W.-H. Lai and M. Shao, Sustainable and High-Rate Electrosynthesis of Nitrogen Fertilizer, *Angew. Chem., Int. Ed.*, 2023, **62**, e202307123.
43 Q. Wu, C. Dai, F. Meng, Y. Jiao and Z. J. Xu, Potential and electric double-layer effect in electrocatalytic urea synthesis, *Nat. Commun.*, 2024, **15**, 1095.
44 Y. Wang, Y. Wang, Q. Zhao, H. Xu, S. Zhu, F. Yang, E. P. Delmo, X. Qiu, C. Song, J. Jang, T. Li, P. Gao, M. Danny Gu and M. Shao, Efficient C-N coupling in electrocatalytic urea generation on copper carbonate hydroxide electrocatalysts, *J. Energy Chem.*, 2024, **93**, 289–298.
45 T. Niederprüm, O. Thomas, T. Eichert, C. Lippe, J. Pérez-Ríos, C. H. Greene and H. Ott, Observation of pendular butterfly Rydberg molecules, *Nat. Commun.*, 2016, **7**, 12820.
46 V. Lamba, S. J. Wilkinson and C. Arora, Designing molecular devices by altering bond lengths, *J. Mol. Model.*, 2011, **17**, 3251–3255.
47 Y. Wang, T. Liu and Y. Li, Why heterogeneous single-atom catalysts preferentially produce CO in the electrochemical CO_2 reduction reaction, *Chem. Sci.*, 2022, **13**, 6366–6372.
48 J.-C. Liu, F. Luo and J. Li, Electrochemical Potential-Driven Shift of Frontier Orbitals in M–N–C Single-Atom Catalysts Leading to Inverted Adsorption Energies, *J. Am. Chem. Soc.*, 2023, **145**, 25264–25273.
49 J. Liu, P. Li, J. Bi, S. Jia, Y. Wang, X. Kang, X. Sun, Q. Zhu and B. Han, Switching between C_{2+} Products and CH_4 in CO_2 Electrolysis by Tuning the Composition and Structure of Rare-Earth/Copper Catalysts, *J. Am. Chem. Soc.*, 2023, **145**, 23037–23047.
50 K. Kim, B. Koo, Y.-R. Jo, S. Lee, J. K. Kim, B.-J. Kim, W. Jung and J. W. Han, Control of transition metal–oxygen bond strength boosts the redox ex-solution in a perovskite oxide surface, *Energy Environ. Sci.*, 2020, **13**, 3404–3411.
51 Y. Ding, W. Zhou, J. Li, J. Wang, L. Xie, X. Meng, J. Gao, F. Sun, G. Zhao and Y. Qin, Revealing the In Situ Dynamic Regulation of the Interfacial Microenvironment Induced by Pulsed Electrocatalysis in the Oxygen Reduction Reaction, *ACS Energy Lett.*, 2023, **8**, 3122–3130.
52 X. Zhang, H. Sun, Y.-R. Wang, Z. Shi, R.-L. Zhong, C.-Y. Sun, J.-Y. Liu, Z.-M. Su and Y.-Q. Lan, Dynamic Control of Asymmetric Charge Distribution for Electrocatalytic Urea Synthesis, *Adv. Mater.*, 2024, **36**, 2408510.
53 J. Hu, S. Osella, J. Albero and H. García, Ni and Mo atom pairs as single sites on N-doped graphitic carbon for urea formation by simultaneous CO_2 and NO_2^- reduction with pulsed electrocatalysis, *EES Catal.*, 2025, **3**, 1075–1086.
54 H. Sun and J.-Y. Liu, A Pulsed Tandem Electrocatalysis Strategy for CO_2 Reduction, *J. Am. Chem. Soc.*, 2025, **147**, 14388–14400.
55 M. Chen, K. Chang, Y. Zhang, Z. Zhang, Y. Dong, X. Qiu, H. Jiang, Y. Zhu and J. Zhu, Cation-Radius-Controlled Sn–O Bond Length Boosting CO_2 Electroreduction over Sn-Based Perovskite Oxides, *Angew. Chem., Int. Ed.*, 2023, **62**, e202305530.
56 X. Zhao, Z. Li, H. Jang, X. Wei, L. Wang, M. G. Kim, J. Cho, X. Liu and Q. Qin, 2D Ruthenium–Chromium Oxide with Rich Grain Boundaries Boosts Acidic Oxygen Evolution Reaction Kinetics, *Small*, 2024, **20**, 2311172.
57 C. Liu, M. Zhang, J. Li, W. Xue, T. Zheng, C. Xia and J. Zeng, Nanoconfinement Engineering over Hollow Multi-Shell Structured Copper towards Efficient Electrocatalytical C–C coupling, *Angew. Chem., Int. Ed.*, 2022, **61**, e202113498.
58 Y. Shi, Y. Wang, J. Yu, Y. Chen, C. Fang, D. Jiang, Q. Zhang, L. Gu, X. Yu, X. Li, H. Liu and W. Zhou, Superscalar Phase Boundaries Derived Multiple Active Sites in SnO_2/Cu_6Sn_5/CuO for Tandem Electroreduction of CO_2 to Formic Acid, *Adv. Energy Mater.*, 2023, **13**, 2203506.
59 Y. Zhou, H. Cao, Z. An, M. Li, Y. Huo, J. Jiang, J. Xie and M. He, Efficient electrocatalytic CO_2 reduction on $Ti_3C_2O_2$ surfaces: The effect of single-atom TM anchoring on product selectivity, *Appl. Surf. Sci.*, 2023, **616**, 156492.